



Collective motion in hcp-Fe at Earth's inner core conditions

Youjun Zhang^{a,b,1} , Yong Wang^{c,1}, Yuqian Huang^a, Junjie Wang^c, Zhixin Liang^c, Long Hao^d, Zhipeng Gao^d, Jun Li^{d,2}, Qiang Wu^d, Hong Zhang^e, Yun Liu^b, Jian Sun^{c,2} , and Jung-Fu Lin^{f,2}

Edited by Russell Hemley, University of Illinois at Chicago, Chicago, DC; received June 14, 2023; accepted August 15, 2023

Earth's inner core is predominantly composed of solid iron (Fe) and displays intriguing properties such as strong shear softening and an ultrahigh Poisson's ratio. Insofar, physical mechanisms to explain these features coherently remain highly debated. Here, we have studied longitudinal and shear wave velocities of hcp-Fe (hexagonal close-packed iron) at relevant pressure–temperature conditions of the inner core using in situ shock experiments and machine learning molecular dynamics (MLMD) simulations. Our results demonstrate that the shear wave velocity of hcp-Fe along the Hugoniot in the premelting condition, defined as T/T_m (T_m ; melting temperature of iron) above 0.96, is significantly reduced by ~30%, while Poisson's ratio jumps to approximately 0.44. MLMD simulations at 230 to 330 GPa indicate that collective motion with fast diffusive atomic migration occurs in premelting hcp-Fe primarily along [100] or [010] crystallographic direction, contributing to its elastic softening and enhanced Poisson's ratio. Our study reveals that hcp-Fe atoms can diffusively migrate to neighboring positions, forming open-loop and close-loop clusters in the inner core conditions. Hcp-Fe with collective motion at the inner core conditions is thus not an ideal solid previously believed. The premelting hcp-Fe with collective motion behaves like an extremely soft solid with an ultralow shear modulus and an ultrahigh Poisson's ratio that are consistent with seismic observations of the region. Our findings indicate that premelting hcp-Fe with fast diffusive motion represents the underlying physical mechanism to help explain the unique seismic and geodynamic features of the inner core.

Earth's core | high pressure | machine learning molecular dynamics | premelting | collective motion

Seismology and mineral physics studies over the past century reveal that Earth's inner core is mainly made of solid iron (1, 2). The inner core only accounts for less than 1% of the planet's total volume but plays a key role in its dynamics, thermal evolution, core convection, and habitability. Of particular example is its nucleation and light element release to provide thermochemical energy sources powering the geodynamo, the generation of the magnetic field, and subsequent geological processes (3–5). Recent seismological investigations from modern J wave (6) and preliminary reference Earth model (1) have shown that the inner core has a shear wave velocity 30 to 40% lower than expected from solid hcp-Fe (hexagonal close-packed iron) alloy at similar pressure, while the compressional wave velocity is overall consistent with that of the constituent Fe alloy (7, 8). This indicates an ultralow shear modulus in the inner core, with a Poisson's ratio (ν) as high as 0.44 to 0.45, analog to that of soft metals such as lead and thallium (9) and close to that of molten iron ($\nu = 0.5$). The Poisson's ratio of the inner core is much larger than that of hcp-Fe estimated at the core's pressure and room temperature ($\nu \sim 0.35$) (10, 11). These seismic observations, therefore, suggest the existence of an extremely soft solid iron alloy with low rigidity in the inner core (12). This raises the fundamental question about the main underlying physical mechanism responsible for the unique seismic and geodynamic features in the region. Understanding the atomistic dynamics and its influence on the longitudinal (V_p), bulk (V_b), and shear (V_s) sound velocities of iron at Earth's inner core conditions can greatly enhance our knowledge of the inner working of our planet (13–15).

Driven by the continuous cooling of the planet, the solidification of the inner core occurs when its adiabat intersects the melting curve of the constituent iron alloy at the inner core boundary (ICB) (16). Using the melting curve of pure iron as a reference, the melting temperature (T_m) at the ICB is determined to be ~6,200(300) K at 330 GPa by experiments (17–21) and theories (22, 23). Addition of a few percent of light element(s) in iron is expected to depress the melting temperature by several hundreds of K (24). According to an isentropic modeling, the temperature gradient across the inner core radius (r), dT/dr , is expected to be approximately -0.17 K/km (16). This suggests that the temperature increase is only 100 to 200 K from the ICB to the center across a radius of ~1,200 km. As a result, the inner core adiabat is expected to be within the temperature regime T/T_m exceeding approximately

Significance

Earth's solid inner core exhibits intriguing characteristics such as an exceptionally low shear-wave velocity and an ultrahigh Poisson's ratio. In this study, we have used high pressure–temperature experiments and machine learning calculations to examine the dynamics and sound velocities of hcp-Fe (hexagonal close-packed iron) at the inner core conditions. Our research reveals a drastic reduction in shear wave velocity when hcp-Fe approaches the melting point. Our advanced calculations show that iron atoms display collective motion with fast diffusion in the premelting regime, leading to the ultralow shear modulus and ultrahigh Poisson's ratio. These results are consistent with seismic observations and geodynamics of the inner core, demonstrating that collective motion in hcp-Fe softens Earth's solid inner core.

Author contributions: Y.Z. designed research; Y.Z., Y.W., Y.H., J.W., Z.L., L.H., Z.G., J.L., Q.W., H.Z., Y.L., J.S., and J.-F.L. performed research; Y.Z. and Y.W. contributed new reagents/analytic tools; Y.Z., Y.W., J.S., and J.-F.L. analyzed data; and Y.Z., Y.W., J.S., and J.-F.L. wrote the paper.

The authors declare no competing interest.

This article is a PNAS Direct Submission.

Copyright © 2023 the Author(s). Published by PNAS. This article is distributed under [Creative Commons Attribution-NonCommercial-NoDerivatives License 4.0 \(CC BY-NC-ND\)](https://creativecommons.org/licenses/by-nc-nd/4.0/).

¹Y.Z. and Y.W. contributed equally to this work.

²To whom correspondence may be addressed. Email: lijun102@caep.cn, jiansun@nju.edu.cn, or afu@jsg.utexas.edu.

This article contains supporting information online at <https://www.pnas.org/lookup/suppl/doi:10.1073/pnas.2309952120/-/DCSupplemental>.

Published October 2, 2023.

0.95. As the temperature approaches T_m , a previous study has suggested that some solids can show premelting behaviors with collective motion and fast atomic diffusion (25). Theoretical simulations have predicted that unusual elastic and rheological properties occur in several metals like Cu, Al, Ta, and Ca at the premelting temperature (26–28). This raises the possibility that premelting iron at T/T_m above 0.95 and inner core pressures can exhibit unique elastic and rheological characteristics manifested in the aforementioned seismic observations.

To date, several hypotheses have been proposed to explain the observed seismic features in the inner core (7, 29–32). A pioneering study on the elasticity calculations of hcp-Fe predicted a strong shear softening at high P–T (pressure–temperature) prior to melting (30), suggesting that premelting hcp-Fe may exhibit distinct behavior from ideal hcp-Fe. However, the simulation was conducted using relatively short simulation time and small cell size under homogeneous melting with superheating effects (>7,500 K at the ICB pressure where iron is expected to be molten) (30). On the other hand, first-principles DFT (density-functional-theory) calculations showed that the shear modulus of hcp-Fe decreases quasi-linearly with temperature at a given density and agrees with the seismology and free oscillation data for the inner core without the requirement of premelting behavior (33, 34). Numerous high P–T experiments and modeling studies on the strength and plastic deformation have suggested that hcp-Fe is rheologically weak with a low shear strength due to pressure-induced slip and creep, and its shear strength could be reduced by the elevated temperature (35–39). However, these experiments were conducted at P–T conditions far below those of the inner core. Furthermore, some high-pressure experiments and molecular dynamic (MD) computations indicate that iron carbide [e.g., Fe₇C₃ compound (31)] or iron–hydrogen superionic alloy (32, 40) can reduce the shear wave velocity of the inner core. However, it is still highly controversial whether C and/or H light elements exist in Earth's inner core (24). Bcc-Fe has also been proposed as a possible explanation for the origin of the low shear wave velocity in the inner core (41–43), but in situ x-ray diffraction (XRD) experiments did not observe its existence at the relevant P–T conditions (19, 20, 44). Possible presence of melt pockets in the inner core has been suggested as an explanation for the high Poisson's ratio (45), although the inner core growth models indicate that interstitial liquid would have been squeezed out during its complete solidification and compaction below the solidus (46). Insofar, these existing hypotheses could help address some aspects of the inner core's unique properties, but a comprehensive physical model incorporating direct experimental elasticity data and theoretical simulations with large supercells remains lacking.

Iron is believed to be stable in the hcp structure under the inner core P–T conditions as revealed by both static (18, 44) and dynamic (19, 20) experiments. Several experimental investigations on the density, sound velocities, and Poisson's ratio of hcp-Fe have been carried out (29, 47–54); however, some experiments were conducted at relatively low P–T conditions [e.g., up to ~73 GPa and 1,700 K (29); up to ~300 GPa at room temperature (50, 51)] or did not reach to the temperature prior to melting points [e.g., static (49) and shock (53) experiments]. In this study, we have performed direct shock-wave measurements and machine learning (ML)-enhanced simulations with supercell sizes of more than 10,000 atoms to investigate the V_p , V_b , and V_s of compressed hcp-Fe near the premelting temperature at the core pressure. Our theoretical results suggest that collective atomic motion occurs in premelting hcp-Fe, causing a strong sound velocity softening and enhanced Poisson's ratio. The collective motion-induced elastic

softening in hcp-Fe is proposed to be the underlying physics to explain the unique seismic features of the inner core, including its ultralow shear wave velocity, low rigidity, and ultrahigh Poisson's ratio.

Results and Discussion

High P–T shock compression experiments were conducted on high-purity polycrystalline iron (>99.98%) using a hypervelocity reverse-impact technique in two-stage light-gas guns (*Materials and Methods* and *SI Appendix*, Fig. S1). Iron was shock-compressed to pressures ranging from 82 to 231 GPa and temperatures ranging from 1,600 to 5,220 K along its Hugoniot P–T curve, where the shock Hugoniot temperature has been well determined by both experiments and simulations (17, 19, 23, 52) (*SI Appendix*, Table S1 and Fig. S8). The most recent shock compression experiments coupled with in situ XRD indicate that the hcp-Fe should be the only phase present at pressures between 200 and 1,000 GPa prior to melting (19, 20). In this work, we targeted a maximum single shock pressure just below the pressure at which shock-induced melting occurs (~242 GPa) (19). Therefore, iron should be in the hcp structure at the present investigated P–T range. We then obtained the (Eulerian) sound velocities of hcp-Fe including V_p , V_b , and V_s under shock compression by solving the relationship among time interval, wave speed, and distance (*SI Appendix*, Figs. S2–S4).

Analysis of the shock experimental results indicates that the V_p of hcp-Fe linearly increases with increasing shock pressure (P_H) between 80 and 160 GPa (Fig. 1A). After further shock pressure increase, the rate of change in V_p with respect to P_H (dV_p/dP_H) gradually decreases and eventually changes to a negative slope above ~206 GPa. Additionally, the V_b in shock-compressed iron shows a monotonous increase from 82 to 231 GPa. Our measured V_p are generally consistent with those of shock-compressed iron in refs. 48 and 53, while we did not observe a sharp discontinuity of V_p at 200 to 220 GPa as reported earlier that was explained as a solid–solid phase transition from hcp to a new phase (47). Our V_p results at relatively low P–T conditions agree well with an earlier report (49) on hcp-Fe up to ~163 and 3,000 K using inelastic x-ray scattering (IXS) in laser-heated diamond anvil cells (LH-DACs) (Fig. 1A). Both sets of results support the notion that the V_p of hcp-Fe exhibits a quasi-linear relationship with density in this P–T range (49). However, our results suggest that as the P–T conditions approach the region of shock-induced melting, the sound velocity of hcp-Fe has a nonlinear relation with density and does not follow the quasi-linear sound velocity–density relationship (*SI Appendix*, Fig. S9). Our measured V_s of iron under shock compression shows a gradual increase with pressure and density from ~80 to 160 GPa but stops to increase above 160 GPa. At shock pressures above 200 GPa, the V_s of iron displays a dramatic drop from 4.2 km/s to zero as iron melts along the Hugoniot (Fig. 1A and *SI Appendix*, Fig. S9).

Under shock compression, both pressure and temperature is simultaneously elevated along the Hugoniot, which could affect the sound velocities of hcp-Fe in a different way. High P–T experiments in externally/laser-heated DACs have shown that the V_p and V_s of hcp-Fe generally increase with pressure but decrease with temperature (29, 54). Therefore, we have further investigated the effect of the shock Hugoniot temperature (T_H) on the sound velocity of hcp-Fe using the recently developed optical pyrometry technique (17). These results show that T_H in hcp-Fe increases monotonously from approximately 1,600 to 5,220 K as pressure increases from 82 to 231 GPa (*SI Appendix*, Fig. S8). Based on a consensual melting curve of hcp-Fe (17–21), we calculated its

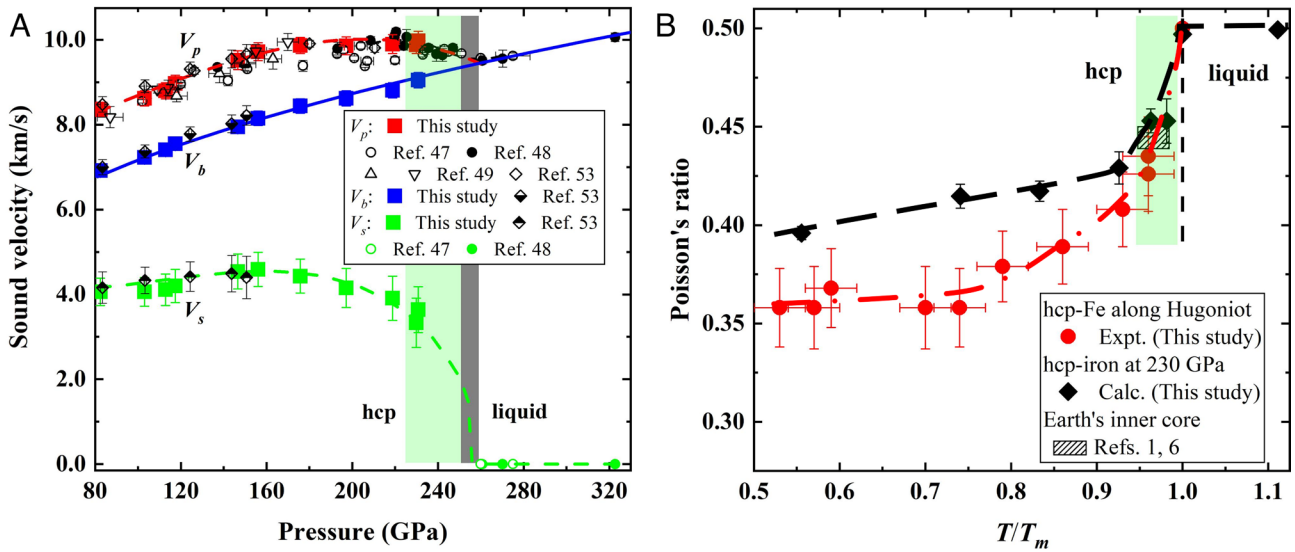


Fig. 1. Sound velocities and Poisson's ratio of iron along the shock Hugoniot conditions. (A) Measured sound velocities V_p (red squares), V_b (blue squares), and V_s (green squares) of iron under shock compression. Solid (48) and open (47) circles are the measured V_p under shock compression from the literature results. Diamonds, diamonds with bottom half black, and diamonds with top half black represent the measured V_p , V_b , and V_s , respectively, under shock compression by ref. 53. The triangles and inverted triangles represent the measured V_p of hcp-Fe at given pressures and $\sim 3,000$ and $2,300$ K, respectively, using IXS in LH-DACs (49). The blue line represents the calculated V_b of iron using a thermodynamic equation under shock compression. The red dashed line in V_p was fitted to the measured data using a third-order polynomial and is meant as a guide for the eye. The green dashed line through the experimental data in V_s is derived from V_p and V_b . The vertical gray bar represents the pressure range for iron melting to occur along the shock Hugoniot. (B) Measured and calculated Poisson's ratio of hcp-Fe as a function of the ratio of temperature to the melting point of iron (T/T_m). By definition, the Poisson's ratio reaches 0.5 at T/T_m of 1.0 in molten iron (horizontal dashed black line). The Poisson's ratio of the inner core constrained by seismic observations falls within the range of 0.44 to 0.45 (striped rectangle region) (1, 6), which is located at $T/T_m \sim 0.96$ for hcp-Fe at high pressure. The difference in Poisson's ratio between experimental and computational results at relatively low T/T_m may be attributed to the pressure difference between Hugoniot conditions in experiments and isobaric conditions in calculations. The light-green region indicates a significant shear softening and ultrahigh Poisson's ratio induced by collective atomic motion in hcp-Fe at shock pressures above ~ 230 GPa and T/T_m greater than ~ 0.96 .

ratio of shock Hugoniot temperature to the melting point, T_H/T_m , which gradually increases from 0.44 to 0.96 with shock pressure from 82 to 231 GPa (SI Appendix, Table S1). We note that the V_s stops to increase at shock pressures above approximately 160 GPa, where the T_H/T_m approaches ~ 0.74 . At P-T conditions further up to ~ 230 GPa, with a solid Hugoniot temperature close to the melting point ($T_H/T_m \sim 0.96$), the V_s values drastically drop by approximately 30% (Fig. 1A). Our shock results reveal that the V_s of hcp-Fe at $T_H/T_m \sim 0.96$ to 1.00, which we define as the premelting region, displays a strong temperature-dependent reduction. This dramatic drop in the measured V_s agrees with some previous theoretical predictions by ab initio MD (AIMD) simulations (30), which shows a strong nonlinear elastic constant weakening in hcp-Fe just before melting.

Based on our measured V_p , V_b , and V_s along the Hugoniot, the derived Poisson's ratio of iron increases from ~ 0.34 to 0.43 as shock pressure increases from ~ 82 GPa (1,600 K) to 231 GPa (5,220 K), as shown in Fig. 1B. At conditions below ~ 160 GPa and 3,450 K (with T_H/T_m less than ~ 0.74), the Poisson's ratio appears to be comparable to that of hcp-Fe at high pressure and room temperature (~ 0.35), as observed in DAC experiments (10, 11) (Fig. 1B), suggesting that temperature has only a minor effect at relatively low values of T_H/T_m . Furthermore, static high-pressure experiments demonstrate that the Poisson's ratio of iron does not significantly change with increasing pressure to the cores at room temperature (10, 11), indicating that the rise in shock-compressed iron up to 230 GPa should be mainly due to shock-induced high temperatures. When compared to seismic observations, the Poisson's ratio of 0.43 in hcp-Fe at $T_H/T_m \sim 0.96$ and $P_H \sim 230$ GPa is generally consistent with the ratio of ~ 0.44 to 0.45 in the inner core (the striped rectangle area in Fig. 1B).

To gain insight into the atomistic behavior and lattice dynamics of premelting hcp-Fe, we developed a ML potential with DFT

accuracy, using the deep concurrent learning method (Materials and Methods and SI Appendix, Figs. S5–S7). Equilibrium and nonequilibrium MD simulations (EMD and NEMD) were conducted at pressures ranging from 230 to 330 GPa and at various temperatures, up to the nanosecond simulation scale. At temperatures close to the melting point ($T/T_m > \sim 0.96$), we observed the spontaneous emergence of atomic collective motion in hcp-Fe, along its [100] or [010] crystallographic orientation, where Fe atoms diffuse collectively in both intralayer and interlayer directions (Fig. 2A and Movie S1). Specifically, most atoms exhibit a one-dimensional (1-D), longitudinal wave-like behavior in open-loop (chain-like) diffusions, wherein one atom jumps out of its equilibrium position and pushes its neighboring atoms along specific crystallographic directions, such as [100] or [010] in the a–b plane (Fig. 2B). This collective motion generates a wavefront of diffusion, moving randomly forward until it meets a vacancy and releases the compression. This phenomenon previously reported for premelting cubic Ca at high pressure has been suggested to be a prevalent high P–T feature in metals (28). The longitudinal-wave-like behavior could dissipate shear in the system at the atomistic level, which was also observed in the premelting bcc-Ta (55) and fcc-Al (56) at ambient pressure.

The distribution of iron atomic displacements is also investigated within a given lag time (up to 0.1 ns) using time-dependent van Hove self-correlation functions $P(\Delta r, t)$ (57, 58). At the V_s softening regime (e.g., $T/T_m \sim 0.98$), hcp-Fe atoms migrate collectively to their neighboring lattice points. This migration leads to a non-Gaussian multiple-peak distribution of $P(\Delta r, t)$ (horizontal dashed-line in Fig. 2C). However, in solid hcp-Fe at a relatively low temperature below the region (e.g., $T/T_m \sim 0.92$), $P(\Delta r, t)$ exhibits a stable Gaussian distribution over time in the nanosecond-scale simulation, indicating the absence of collective motion (SI Appendix, Fig. S11).

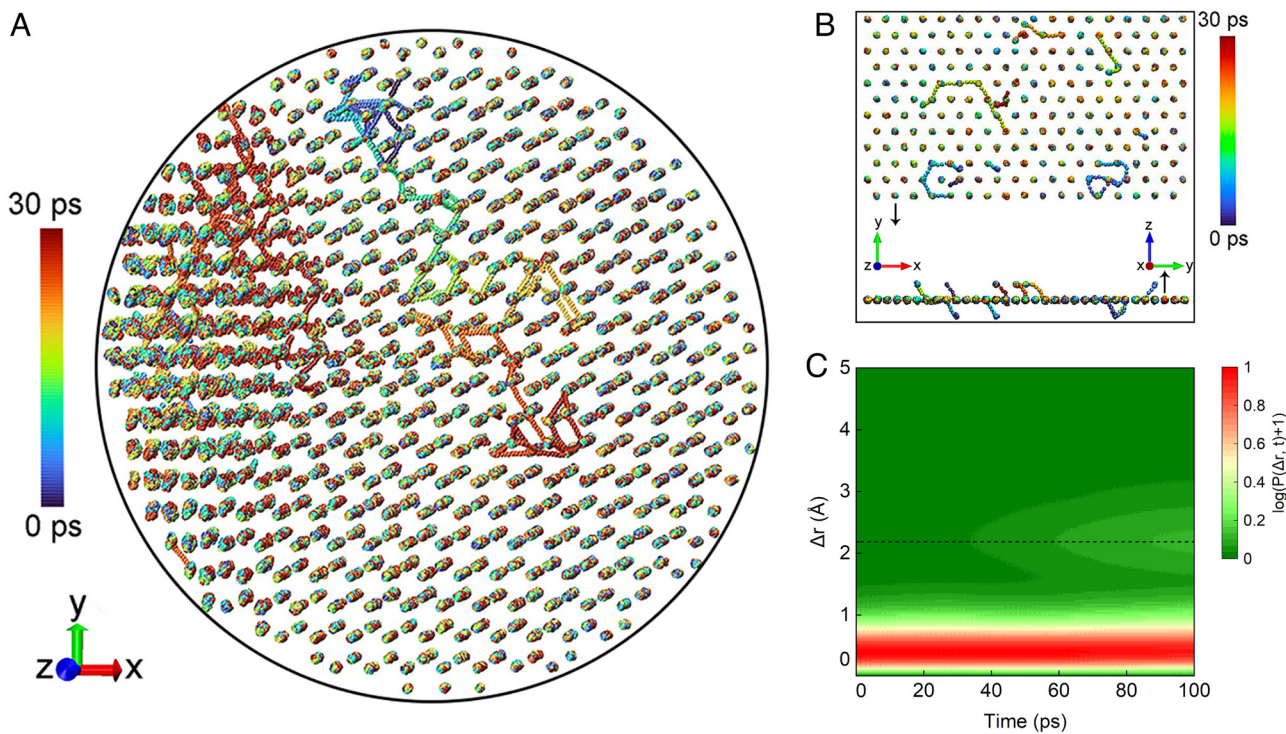


Fig. 2. Collective atomic motion of compressed hcp-Fe at near melting point and 230 GPa. (A) Dynamic behavior of hcp-Fe atoms at 230 GPa and near melting temperature ($T = 5300$ K and $T/T_m \sim 0.98$) using MLMD. Iron atoms are colored with time over a 30-ps period in the snapshot. (B) Top- and side-view dynamical snapshots of a single close-packed a-b (x - y) plane during 30 ps in premelting hcp-Fe with collective motion. Iron atoms predominantly diffuse along [100] or [010] directions of the hcp structure. This diffusion leads to the formation of open-loop strings and a few closed-loop shapes such as triangular. The open-loop diffusion behavior propels iron atoms to form a 1-D longitudinal wave-like pattern. Snapshots in (A) and (B) were smoothed within a 1-ps time window to eliminate thermal noises. (C) Van Hove self-correlation function $P(\Delta r, t)$ of premelting hcp-Fe. Iron atoms migrate to neighbors during collective atomic motion, which induces multiple-peak non-Gaussian distribution vs. time in the correlation functions. The $P(\Delta r, t)$ represents the probability of finding an atom at distance Δr after a time interval t . The vertical bar represents the logarithm form of the $P(\Delta r, t)$ to highlight the diffusion of collective motion (marked by the black dashed line as the nearest neighbor distance).

Furthermore, we computed the mean square displacements (MSD) for hcp-Fe at different temperatures and found that the MSD of premelting hcp-Fe at 230 GPa and 5,300 K ($T/T_m \sim 0.98$) steadily increases throughout 250 ps simulation time. This means that collective motion contributes to significant diffusion of atoms (Fig. 3A). Notably, the average diffusion in the a-b planes of premelting hcp-Fe spreads faster than that along the c-axis. Conversely, at a relatively low temperature of 4,000 K ($T/T_m \sim 0.74$) at 230 GPa, the MSD of hcp-Fe atoms remains nearly constant during the simulation time, indicating no observable diffusion (Fig. 3A).

For a deeper understanding of the collective atomic motion in premelting hcp-Fe, we have theoretically investigated its finite-temperature phonon dispersions including the anharmonicity and enthalpy at 230 GPa and various temperatures (Fig. 3B). Our calculations show abnormal softening in some high symmetry points at high P-T (Fig. 3B), corresponding to the relative vibrations between close-packed planes along the c-axis in hcp structures (Fig. 3C). These softening reflect temperature effects as a dynamical driving force for collective atomic motion, which mostly diffuses between the close-packed planes of hcp-Fe. From an energetic perspective, the mixture of solid and liquid near melting promotes disorders and increases the system's potential energy compared to an ideal hcp-Fe crystal. However, the directional priority of collective motion pushes atoms to diffuse along the lowest energy paths, which only slightly increases the system's enthalpy compared to ideal hcp-Fe without collective motion (Fig. 3D). Given the complexity of the potential energy surface (PES) at high temperatures and the large entropy induced by the collective motion, hcp-Fe with collective motion may be dynamically stable in the premelting P-T conditions.

To investigate how collective atomic motion affects physical properties of hcp-Fe, we conducted calculations on its elastic constants and Poisson's ratio at high P-T. It should be noted that traditional elastic modulus calculations using the EMD method for single crystal hcp-Fe are susceptible to superheating effects. To overcome this, we employed a solid defective structure quenched from the two-phase model in NEMD simulations to mitigate the impact of superheating in order to accurately calculate the high P-T elastic constants (SI Appendix). Results from both the ab initio method and the constructed ML model show that a significant shear elastic softening occurs in hcp-Fe at 230 GPa as the temperature approaches the melting point, consistent with the present experimental observations (Fig. 4). The present calculations and experiments indicate that the shear modulus of hcp-Fe at 230 GPa and $T/T_m \sim 0.96$ to 0.98 agrees overall with the seismically observed low shear modulus of the inner core (Fig. 4). Furthermore, the calculated Poisson's ratio using NEMD increases from 0.36 to 0.42 as the temperature rises from 300 to 5,000 K ($T/T_m \sim 0.92$) at 230 GPa (Fig. 1B). When the temperature continues to rise from 5,000 K to the melting point at 5,400 K, the Poisson's ratio of hcp-Fe increases dramatically from 0.42 to 0.5. Our computations reveal that the Poisson's ratio in hcp-Fe with collective motion is approximately 0.45 at 230 GPa and 5,200 K ($T/T_m \sim 0.96$), which is overall consistent with our experimental value at similar P-T conditions (Fig. 1B).

We conducted more calculations at pressures ranging from 230 to 330 GPa and temperatures between 4,000 and 7,000 K to determine the P-T regime of hcp-Fe with collective motion at relevant inner core conditions. Our results reveal the dynamic phase boundary between ideal hcp-Fe and hcp-Fe with collective

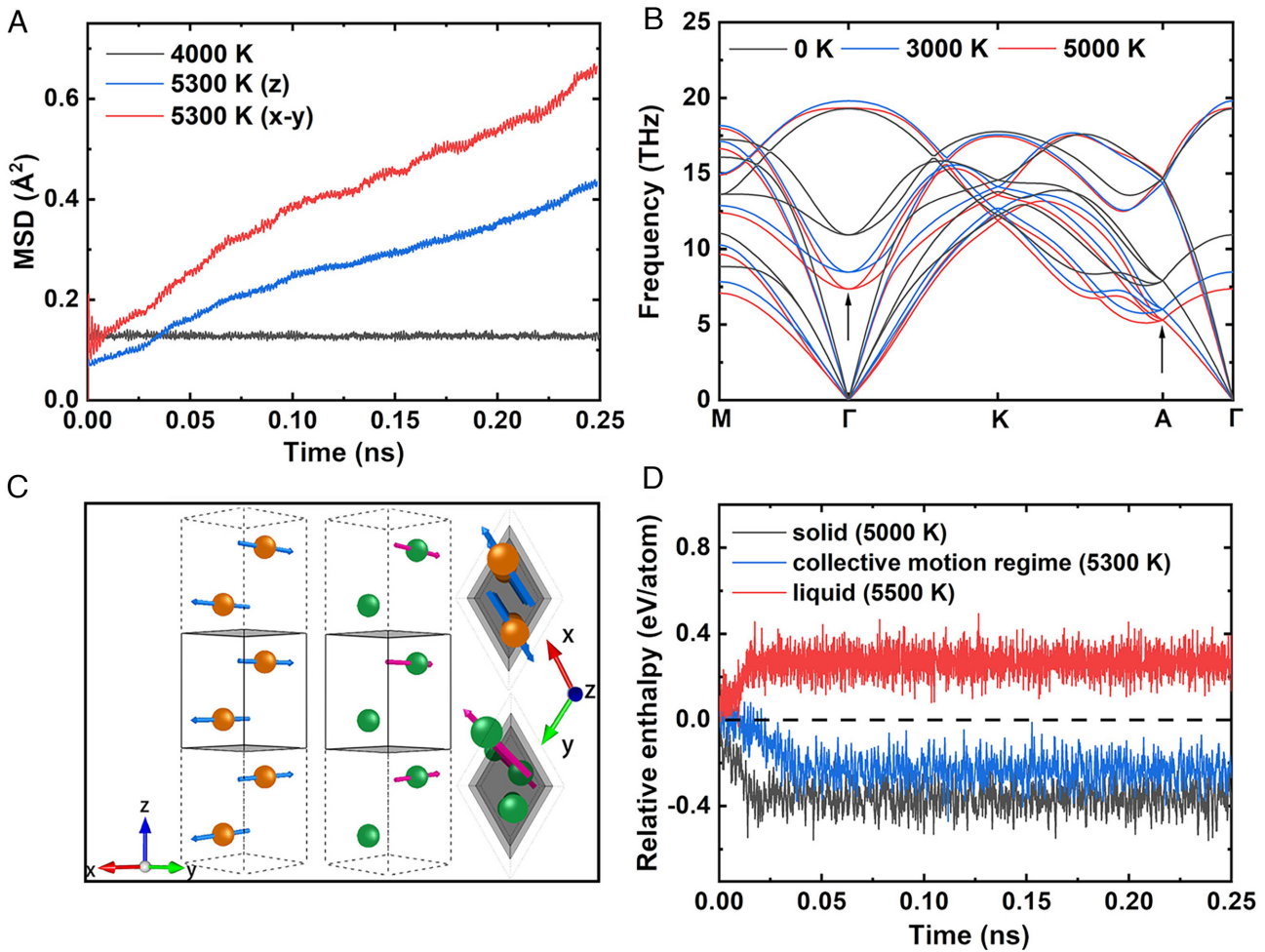


Fig. 3. Dynamical properties of hcp-Fe at ~ 230 GPa and representative temperatures. (A) Calculated MSD of hcp-Fe atoms at 230 GPa and varied temperatures. The atoms in premelting hcp-Fe diffuse with the simulation time. The diffusion of hcp-Fe atoms primarily occurs in the a - b planes as they migrate to neighboring atoms. Diffusion in the z -direction is usually triggered by the vacancies' migration between different a - b planes, of which vacancies were made by the collective motion in a - b planes. (B) Phonon spectra of hcp-Fe at 230 GPa and three given temperatures (0 K, 3,000 K, and 5,000 K). Anharmonicity is taken into consideration in the calculations. Black arrows highlight some modes in the phonon spectra that show strong softening as the temperature increases. (C) Schematic diagram of the softening direction of hcp-Fe at high P-T. Blue arrows through orange atoms show a strong phonon softening in the Γ point of hcp-Fe reduced from ~ 12 THz at 0 K to ~ 7 THz at 5,000 K and at 230 GPa, where the vibrational direction is between adjacent a - b close-packed planes. Magenta arrows through green atoms show a similar softening direction in the A (0, 0, 0.5) point, where the softening happens between nonadjacent planes. (D) Enthalpy of iron in hcp, hcp with collective motion, and liquid states, respectively, at 230 GPa as a function of simulation time. Systems evolve from the initial solid-liquid mixture to hcp crystal at 5,000 K ($T/T_m \sim 0.92$), to hcp with collective motion at 5,300 K ($T/T_m \sim 0.98$), and to liquid at 5,500 K ($T/T_m \sim 1.02$), respectively. The horizontal dashed line represents the initial enthalpy of the solid-liquid mixture (*SI Appendix, Fig. S7*).

motion as well as the boundary between hcp-Fe and liquid Fe (Fig. 5). We found that the temperature for hcp-Fe with collective motion (T_c) extends approximately 500 K below its T_m at inner core pressures. Comparison between our predicted dynamic phase of hcp-Fe with collective motion and a typical adiabat of the iron core indicates that the inner core adiabat is slightly below the T_m and falls within the temperature region of premelting hcp-Fe with collective motion (Fig. 5 and *SI Appendix, Fig. S13*). As mentioned in the introductory paragraphs, the T/T_m of the inner core is expected to be between 0.95 and 0.99 (16, 46). Our results indicate that the dynamics of collective motion in the premelting hcp-Fe at the conditions relevant to the inner core may be the primary physical mechanism behind the observed seismic properties, such as the ultralow shear wave velocity, low rigidity, and ultrahigh Poisson's ratio (6).

Earth's inner core also contains ~ 5 wt.% Ni and ~ 4 wt.% light element(s) alloyed with iron, though the exact identity of the major light element remains uncertain (24). Here, we consider Si as a candidate light element as an example to understand light element effects on T_m depression and associated elasticity. Addition

of 4 wt.% of Si in Fe or Fe-Ni alloy would lower the melting temperature to a T_m of $\sim 5,800$ K (59) and overall increase the V_p by 3 to 5% (50, 54, 60, 61). Meanwhile, Fe alloyed with ~ 5 wt.% Ni and a few % of Si would retain the hcp structure at relevant inner core P-T conditions (62–64). Using a temperature gradient of 100 to 200 K in the inner core, we estimated that the expected inner core adiabat for iron alloyed with a few wt.% light elements would have a T/T_m of ~ 0.97 to 0.98, which falls within the premelting region ($T_c/T_m > \sim 0.95$). These results suggest that such an Fe-Ni-light element alloy can also exhibit collective atomic motion, resulting in the ultralow shear wave velocity and ultrahigh Poisson's ratio of the inner core.

Our research into the effects of collective atomic motion on premelting hcp-Fe has yielded exciting results regarding its shear softening and ultrahigh Poisson's ratio. These findings provide a physical mechanism to explain the unique seismic and geodynamic features of Earth's solid inner core. The ultralow shear modulus in premelting hcp-Fe suggests that the inner core may have relatively low shear viscosity, making it susceptible to deformation and convectively instability (65). Future high P-T experimental and theoretical studies on

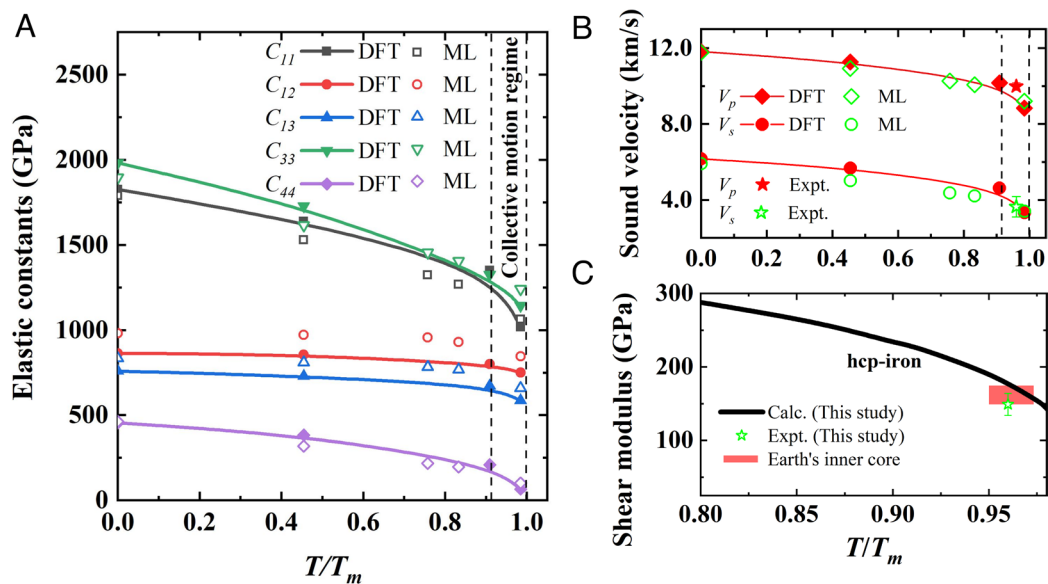


Fig. 4. Elastic constants, sound velocities, and shear modulus of hcp-Fe as a function of the ratio of temperature to its melting point (T/T_m) at 230 GPa. The elastic constants were calculated using both the DFT-AIMD and ML method. (B) Comparisons of sound velocities of hcp-Fe between theoretical and experimental results at high temperatures and 230 GPa. Solid and open symbols represent the results from the DFT-AIMD and ML calculations, respectively, in this study. The melting point T_m of iron at 230 GPa is calculated to be $\sim 5,400$ K by two-phase methods (SI Appendix, Fig. S8). The region between vertical dashed lines covers the premelting condition. The calculated longitudinal and shear wave velocities are consistent with our experimental results at ~ 230 GPa and $T/T_m \sim 0.96$. The shear softening emerges near melting, which is accompanied by collective motion in the large spatiotemporal MLMD (Movie S1). (C) Calculated (black curve) and measured (open star) shear modulus of hcp-Fe at high temperatures and 230 GPa. The shear modulus of premelting hcp-Fe at the relevant conditions of the core can overall match with the seismic observation of 149 to 176 GPa (red region) in the inner core (red bar) (1, 6).

iron alloyed with approximately 5 wt.% nickel and ~ 4 wt.% light elements are needed to address the alloying effects on the premelting regime and behavior under the inner core conditions. We also note that the classical nucleation theory does not consider the potential effects of premelting on material properties (26–28) such as the

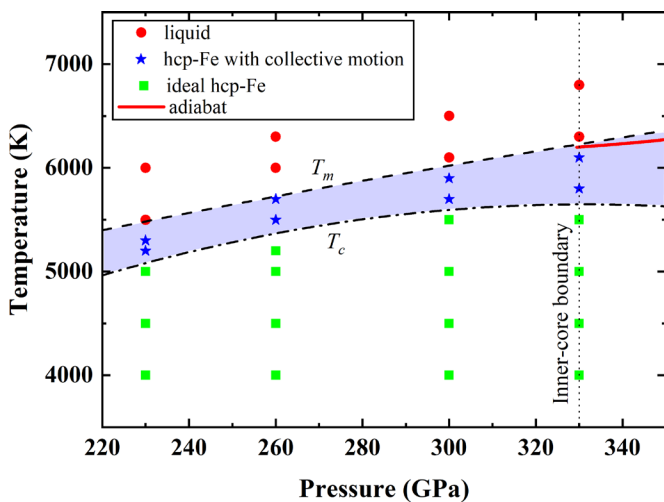


Fig. 5. Predicted dynamic phase boundary of hcp-Fe with collective atomic motion at high P-T conditions relevant to the Earth's core. The dashed line represents the melting curve (T_m) of iron at high pressures in this study fitted by the Simon-Glatzel law with $T_m = T_0 (P/11.8 + 1)^{0.367}$, where $T_0 = 1,811$ K is the melting point of iron at ambient pressure. Our calculated melting points of iron are generally consistent with recent experimental results at relevant P-T conditions of the inner core where the melting point of hcp-Fe is $\sim 6,200$ K and the pressure of the ICB is ~ 330 GPa (SI Appendix, Fig. S8) (17–21). The dash-dotted line represents the dynamic phase boundary between ideal hcp-Fe and hcp-Fe with collective motion (T_c) in this study fitted by a second-order polynomial. The light-blue area represents the predicted P-T conditions of hcp-Fe with collective motion. The red curve represents a typical adiabat of iron anchored at the ICB. The adiabat gradient across the ICB is approximately 0.17 K/km based on isentropic modeling (16).

elasticity. Therefore, further research is required to delve into the various materials properties throughout the premelting regime.

Materials and Methods

Starting Materials. High-purity polycrystalline bulk iron with a purity greater than 99.98% was used as the starting material. The iron samples were prepared into 0.662-mm to 1.480-mm-thick disks with a diameter of ~ 24 mm, and their surfaces were polished to a mirror finish with a roughness of ~ 15 nm (17).

Sound Velocity Measurements and Poisson's Ratio of hcp-Fe at High P-T. Reverse-impact experiments (SI Appendix, Fig. S1) were carried out at both Sichuan University and Institute of Fluid Physics in China. We employed both lithium fluoride (LiF) crystal with $\langle 100 \rangle$ orientation and sapphire Al_2O_3 crystal with $\langle 0001 \rangle$ orientation as window materials, respectively. The interface particle velocity profile was measured using photon Doppler velocimetry (PDV) with a laser wavelength of 1,550 nm and a time resolution of less than 1 ns. The impact velocity was measured using an electromagnetic method with an uncertainty of $\sim 0.5\%$. In the first series of runs, we used LiF crystals with $\langle 100 \rangle$ orientation as the transparent window (66), where the particle velocity profile was recorded at the sample/window interface. This allowed us to generate P-T conditions up to ~ 156 GPa and $\sim 3,400$ K with the highest impact velocity being 7.472(37) km/s. To achieve higher pressures, we employed Al_2O_3 crystals with $\langle 0001 \rangle$ orientation as the window material in the second series of runs because it is denser than LiF crystal and can generate much higher P-T on reverse impact. Even after the phase transformation to CaIrO_3 , Al_2O_3 crystal remained transparent up to at least 210 GPa, and its refractive index under shock compression was recently determined (67). Iron was shocked to Al_2O_3 crystal up to the impact velocity of 7.695(30) km/s, reaching in the highest P-T of ~ 230.8 GPa and $\sim 5,220$ K in this study. The particle velocity wave profiles for these shots are shown in SI Appendix, Fig. S2.

To ensure experimental accuracy, we used four PDV probes to simultaneously measure the particle velocity profiles at four different locations of the sample in a shot (SI Appendix, Fig. S3): One probe was positioned at the center of the impact surface, while the other three were located at the outer ring with a diameter of 5 mm. The wave profiles recorded by multiple probes almost overlapped in one shot, indicating low uncertainty in the sound velocity measurements ($< 3\%$). The

Lagrangian longitudinal sound velocity of iron, C_l , can be directly obtained using the measured time interval (Δt) and the thickness of the sample (δ):

$$C_l = \frac{\delta}{(t_1 - t_0) - \delta/U_s} = \frac{\delta}{\Delta t - \delta/U_s}. \quad [1]$$

Then, the Eulerian longitudinal sound velocity, V_p , which accounts for the change of sample thickness due to shock compression (68), is

$$V_p = \frac{\rho_0}{\rho_H} C_l = \frac{\rho_0}{\rho_H} \frac{\delta}{(t_1 - t_0) - \delta/U_s}, \quad [2]$$

where ρ_0 and ρ_H are the starting and compressed densities of iron and U_s represents the shock wave velocity in shock-compressed iron. The time interval is represented by $\Delta t = t_2 - t_1$. t_1 and t_2 is the time of impact and the arrival of the release wave at the impact interface, respectively, which can be obtained from the measured interface particle velocity profile (SI Appendix, Figs. S2 and S3). The Lagrangian bulk sound velocity (C_b) at the Hugoniot state can be determined by linearly extrapolating the plastic unloading part of the C_l line to the Hugoniot state (SI Appendix, Fig. S4). The elastic-plastic transition point at time t_2 can be identified by calculating the derivative of particle velocity with respect to time (SI Appendix, Fig. S3). The Eulerian bulk sound velocity V_b is obtained by substituting t_1 with t_2 in Eq. 2 (53). By using V_p and V_{br} , the shear wave velocity, V_s , can be obtained using the following relation:

$$V_s^2 = \frac{3}{4} (V_p^2 - V_{br}^2). \quad [3]$$

The reverse-impact experiments (69–71) do not require the fitting of the overtake ratio of sample plate thickness to impactor plate thickness, which differs from symmetric impact experiments previously used (47, 48). Instead, this method directly measures the shock and rarefaction fronts in iron samples, which leads to a significant improvement in the accuracy of sound velocity measurements.

On the other hand, the bulk sound velocity (V_b) of iron under shock compression can be calculated using a thermodynamic equation:

$$V_b^2 = -V^2 \frac{dP_H}{dV} \left[1 - \left(\frac{\gamma}{V} \right) \frac{(V_0 - V)}{2} \right] + V^2 \left(\frac{\gamma}{V} \right) \frac{P_H}{2}, \quad [4]$$

$$P_H = \frac{\rho_0 C_0^2 (1 - \rho_0/\rho)}{[1 - \lambda (1 - \rho_0/\rho)]^2}, \quad [5]$$

where $\rho_0(V_0)$ and $\rho(V)$ are the density (specific volumes) of iron at ambient and shock compression, respectively; γ is the Grüneisen parameter of iron along the Hugoniot state (17, 72); C_0 and λ are the Hugoniot parameters, where U_s (km/s) = 3.935 + 1.578 with $\rho_0 = 7.850(2)$ g cm⁻³ for iron (73). The V_p of hcp-Fe is significantly reduced by elevated temperature, especially above $T/T_m > \sim 0.74$ ($P_H \sim 160$ GPa). We used a third-order polynomial to fit the measured V_p with pressure as V_p (km/s) = 6.9 + 0.011 P_H + 1.15E-4 P_H^2 - 4.61E-7 P_H^3 in the investigated pressure range. The fitted curve gives a maximum V_p of ~ 10.02 km/s at ~ 206 GPa.

The Poisson's ratio of iron can be determined from the measured V_p , V_{br} , and V_s in the present work using the following equation:

$$\nu = \frac{1}{2} \left[1 - \frac{1}{(V_p/V_s)^2 - 1} \right] = 1 - \frac{2}{3(V_b/V_p)^2 + 1}. \quad [6]$$

The uncertainty of the measured sound velocities under shock compression was estimated through the uncertainty propagation using

$$\sigma_{V_p} = \sqrt{\left(\frac{\partial V_p}{\partial \delta} \sigma_{\delta} \right)^2 + \left(\frac{\partial V_p}{\partial \Delta t} \sigma_{\Delta t} \right)^2 + \left(\frac{\partial V_p}{\partial U_s} \sigma_{U_s} \right)^2 + \left(\frac{\partial V_p}{\partial \rho_H} \sigma_{\rho_H} \right)^2}, \quad [7]$$

$$\sigma_{V_s} = \sqrt{\left(\frac{\partial V_s}{\partial V_p} \sigma_{V_p} \right)^2 + \left(\frac{\partial V_s}{\partial V_b} \sigma_{V_b} \right)^2}. \quad [8]$$

The uncertainties in the sample thickness (δ) and the travel time of shock wave in the sample (Δt) were measured to be $\sim 0.1\%$ and $\sim 1\%$, respectively. As shown in SI Appendix, Fig. S3, the measured Δt has a generally small error of 1 to 2 ns, with a total time interval of 120 to 330 ns. Based on the Eqs. 2 and 7, the uncertainties of V_p and V_b are estimated to be $\sim 2\%$. The uncertainty of V_s is estimated to be between 5% and 15% by using the Eqs. 3 and 8.

DFT Calculations at Finite Temperature and AIMDs. In this study, DFT calculations, including structure optimizations and AIMD simulations, are carried out by using the Vienna ab initio simulation (VASP) code (74). The projector augmented-wave potentials (75) and the Perdew–Burke–Ernzerhof Exchange–correlation functional (76) were employed in the calculations. Considering extreme P–T conditions, a 750-eV energy cutoff potential with 16 valence electrons was used, which sufficiently avoided any overlapping of core states. To ensure accuracy, all necessary tests were conducted, and the electronic energy was converged within 1 meV per atom. The optimization of hcp-Fe at 0 K was achieved using a primitive cell with a grid density of $0.025 \times 2\pi \text{ \AA}^{-1}$ for k point sampling in the Brillouin zone at 230 GPa. A series of ab initio NPT (constant number of atoms, pressure, and temperature) MD (77) with Langevin thermostat (78) were performed with a time step of 1 fs to access the proper c/a ratio of hcp-Fe at 230 GPa and finite temperature up to melting (3,000 to 10,000 K). The NPT AIMD simulation cells consisted of a $4 \times 4 \times 3$ supercell for the 4-atom C-centered cell in the hcp structure with orthogonal axes and used Γ -point sampling. These data were utilized to train the initial ML model during the Concurrent ML.

Concurrent ML. In this work, we utilized an end-to-end deep learning model called Deep MD (79, 80) to build a PES using a dataset generated by DFT calculations. This model has been applied to various systems and has demonstrated credible results, including high-pressure calcium (28) and water (81). In addition, it is important to note that a high-quality dataset is crucial for effectively training the model and achieving a more accurate representation of the phase space. Recently, a novel learning procedure with on-the-fly properties was proposed (82), which has been dubbed concurrent learning as the data are generated in real time as the training progresses.

We have leveraged our workflow and DFT results to construct a deep learning potential. The construction process involves three parts, as illustrated in SI Appendix, Fig. S5. Initially, we employed data comprising energy, atomic force, and stress from AIMD simulations of perfect hcp-Fe and hcp-Fe with vacancies to train three initial models with different initialized parameters. Subsequently, we utilized these models to explore a much broader phase space, thereby expediting the process. We then applied an error indicator to identify configurations that were inadequately predicted by the initial models. Those configurations were subjected to DFT self-consistent calculations, and the results were integrated into the dataset. With the aid of this improved dataset, we developed models with enhanced predictive capabilities that could better anticipate the phase space. This procedure was iterated several times (in our study, three times) until we had acquired a reliable potential with DFT accuracy, as demonstrated in SI Appendix, Fig. S6. Additionally, in step 2, we investigated various hcp-Fe structures, including perfect crystal, vacancies, twin crystals, grain boundaries, and a mixture of solid and liquid as depicted in SI Appendix, Fig. S7. This rigorous examination guarantees that our models are practical for a variety of applications.

Machine Learning Molecular Dynamics (MLMD). MLMD were carried out using the LAMMPS code, employing periodic boundary conditions and a time step of 1 fs (83). The simulations comprised a range of particle numbers from 6,912 to 80,640 and were conducted for up to ns-scale durations. We tested the fluctuations in temperature and diagonal stress tensors of iron at 230 GPa and various temperatures using ML simulations with different supercell cell sizes ranging from 144 atoms (a typical size in ab initio simulations) to 31,104 atoms (84) (SI Appendix, Fig. S14).

Melting Point Calculation by the Two-Phase Method Using ML. Theoretical determination of the melting point typically involves comparing free energies of solid and liquid phases or employing direct MD. One method for determining the melting point of a substance involves directly heating it from the low-temperature phase until it transforms into a liquid. The temperature at which this transition occurs is typically considered to be the melting point. However, this method tends to overestimate the melting temperature due to the superheating effect. Using this one-phase method, the melting point of iron at 230 GPa was calculated to be $\sim 6,600$ K, which is much higher than the experimental value. Various factors may contribute

to this superheating issue, such as the simulation cells with only a small number of atoms compared to real systems, particularly in DFT calculations. Consequently, in finite-time simulations, this method often lacks the full distribution of phase space, causing the melting of the system to lag behind the temperature rise. Additionally, heating from a perfect solid to melting is an idealized process, with a transition barrier much higher than in real systems with interfaces.

To address this issue, an improved MD method was proposed, called the two-phase method or coexistence melting method (85). This method involves simulating a mixture of solid and liquid at different temperatures, allowing solid and liquid to compete with each other. The addition of liquid broadens the phase-space distribution of the system. As melting occurs, their free energy becomes equal, allowing the solid and liquid to coexist. However, this method requires a larger cell to accommodate two states and is not commonly used in AIMDs. With the aid of ML potential, it is now feasible to construct a large box and simulate the melting behavior of hcp-Fe on a nanosecond scale. Initially, we heated the perfect hcp-Fe with orthogonal axes until it turned into a fully melted liquid. We then integrated it with an initial solid to form a larger supercell, containing up to 80,640 atoms. To avoid any unreasonable structures, like the occurrence of atoms that are too close to each other at the solid-liquid interface, we added a vacuum layer with a thickness of 1 Å to the interface (as illustrated in *SI Appendix, Fig. S7*), which could be relaxed during the following NPT simulations. Using this coexistence box, a series of NPT MLMD simulations were conducted, and the length of the simulations was up to 0.5 ns to ensure proper systems convergence. We then calculated the free energy of the solid and liquid iron at constant pressure and different temperatures. The temperature at which the free energies of solid and liquid iron are equal is known as the temperature of solid-liquid coexistence or the melting point. The melting point of hcp-Fe at 230 GPa was determined to be 5,350 to 5,400 K at 230 GPa and 6,200 to 6,300 K at 330 GPa (asterisks in *SI Appendix, Fig. S8*), below which the collective atomic motion occurs at $T/T_m \sim 0.96$. Our calculated melting point of hcp-Fe at high pressure is close to that of the previous work using a similar two-phase method (23) and is also consistent with that of recent high P-T experiments (17–21).

Van Hove Self-Correlation Functions. The van Hove self-correlation function $P(\Delta r, t)$ gives the probability of an atom at distance Δr after a time interval t . It is defined as

$$P(\Delta r, t) = \frac{1}{N} \left\langle \sum_{i=1}^N \delta \left(r - \left| \bar{r}_i(t_0 + t) - \bar{r}_i(t_0) \right| \right) \right\rangle_{t_0}, \quad [9]$$

where $\bar{r}_i(t_0)$ is the position of i th atom at a time t_0 , N is the number of atoms, and $\langle \dots \rangle_{t_0}$ is the average of time ensemble. In our simulations, we used 0.1-ns trajectories as the lag time t and 0.05-ns trajectories as the time window of ensemble average.

Finite-Temperature Lattice Dynamics. To obtain the 0-K phonon dispersions, lattice dynamics calculations were performed using the phonopy package (86). A $4 \times 4 \times 3$ hcp-Fe supercell, comprising a 2-atom primitive cell and a grid of $0.025 \times 2\pi \text{ \AA}^{-1}$ for k points was utilized in the simulation. The renormalized phonon spectra including anharmonicity and temperature-dependent phonon properties were determined at finite temperature using the dynaphopy package (87). The same iron supercell ($4 \times 4 \times 3$) was used to perform the MLMDs at varying temperatures with a 1-fs timestep and the 50-ps simulation time. The velocity autocorrelation functions via MD were analyzed by projecting them onto the harmonic modes, which were calculated in the 0-K phonon calculations. Further theoretical details can be found in ref. 87. The lattice dynamics calculated using DFT and ML at 0 K are compared in *SI Appendix, Fig. S6E*.

Calculation for Poisson's Ratio in hcp-Fe Near Melting. When stretching or compressing a material, it can undergo changes in both axial and transverse directions, which is referred to as the Poisson effect. Poisson's ratio (ν) quantifies this phenomenon and is defined as follows:

$$\begin{aligned} \epsilon_{axial} &= dl_{axial} / l_{axial} \\ \epsilon_{trans} &= dl_{trans} / l_{trans} \\ \nu &= \frac{-\epsilon_{trans}}{\epsilon_{axial}}, \end{aligned} \quad [10]$$

where l , dl , and ϵ are, respectively, length, changes in length, and strain along transverse and axial (subscript: trans and axial) directions under certain axial stress.

Nonequilibrium MLMD (NEMLMD) calculations were conducted to directly simulate the Poisson effect. The NEMLMD simulations were performed using the LAMMPS code, employing periodic boundary conditions and a time step of 1 fs (ref. 83). In these calculations, tensile stresses were incrementally applied to completely relaxed equilibrium states, derived from two-phase equilibrium MD, to achieve a strain ϵ_{axial} of 0.05 (*SI Appendix, Fig. S10*). Throughout the deformation process, the temperature was regulated using a Nose-Hoover thermostat, while the pressure on those two dimensions perpendicular to the deformation direction remained fixed at 230 GPa. These deformations encompassed the Poisson effect, and the change in volume under the deformation is given by

$$\frac{dV}{V} = \frac{l_{axial} \times l_{trans}^2 \times (1 + \epsilon_{axial}) (1 + \epsilon_{trans})^2 - l_{axial} \times l_{trans}^2}{l_{axial} \times l_{trans}^2}. \quad [11]$$

Combining the definition in Eq. 10, for a very small value of strain (here 0.05 scale), the first-order approximation yields

$$\frac{dV}{V} \approx \epsilon_{axial} + 2\epsilon_{trans} = \epsilon_{axial} (1 - 2\nu) = dl_{axial} / l_{axial} (1 - 2\nu). \quad [12]$$

When the Poisson's ratio ν equals 0.5, the volume remains unchanged by applied stress, rendering the system an incompressible state, such as a liquid. By examining the correlation between dV/V and dl_{axial}/l_{axial} at 230 GPa and various temperatures (*SI Appendix, Fig. S10*), we can ascertain the value of ν through a linear fitting. Utilizing this approach at room temperature, the Poisson's ratio of hcp-Fe at 230 GPa is approximately 0.36, aligning with some previous experimental findings (10, 11). At temperature T/T_m of approximately 0.96 to 0.98, the Poisson's ratio of hcp-Fe at 230 GPa is calculated to be about 0.44(1), which is consistent with the value (~ 0.45) derived from the computed elastic constants using the Voigt average scheme (32) at the similar T/T_m .

Movies and Snapshots of Deep Learning Simulations. Movies and snapshots of deep learning simulations are rendered using visual MD (88) and Open Visualization Tool (OVITO) (89).

Data, Materials, and Software Availability. Six codes were used to obtain results: VASP for ab initio MD (available at <https://www.vasp.at>) (74); LAMMPS for classical MD (available at <http://lammps.sandia.gov>) (83); Deep-MD kit and Deep Generator (DP-GEN) for training ML potential (available at <https://github.com/deepmodeling/deepmd-kit> and <https://github.com/deepmodeling/dpgen>) (80, 82); Phonopy and Dynaphopy for lattice dynamics (available at <https://phonopy.github.io/phonopy> and <http://abelcarreras.github.io/DynaPhoPy>) (86, 87). All other data are included in the manuscript and/or supporting information.

ACKNOWLEDGMENTS. We acknowledge B. Gan, X.H. Li, Y.X. Hua, and Q.M. Wang for their help in the shock experiments. We thank S.P. Grand, Y.G. Li, X.L. Sun, R.E. Cohen, P. Driscoll, X. Dong, and A.F. Goncharov for the fruitful discussion. This work was supported by the National Natural Science Foundation of China (Grant Nos. 42074098, 12125404, 11974162, and 11834006) and the Fundamental Research Funds for the Central Universities (Nanjing University and Sichuan University). J.-F.L. acknowledges support from the Geophysics Program of the NSF, USA (EAR-1901801). The calculations were carried out using supercomputers at the High-Performance Computing Center of Collaborative Innovation Center of Advanced Microstructures, the high-performance supercomputing center of Nanjing University.

Author affiliations: ^aInstitute of Atomic and Molecular Physics, Sichuan University, Chengdu 610065, China; ^bInternational Center for Planetary Science, College of Earth Sciences, Chengdu University of Technology, Chengdu 610059, China; ^cNational Laboratory of Solid State Microstructures, School of Physics and Collaborative Innovation Center of Advanced Microstructures, Nanjing University, Nanjing 210093, China; ^dNational Key Laboratory for Shock Wave and Detonation Physics, Institute of Fluid Physics, China Academy of Engineering Physics, Mianyang 621900, China; ^eCollege of Physics, Sichuan University, Chengdu 610065, China; and ^fDepartment of Earth and Planetary Sciences, Jackson School of Geosciences, The University of Texas at Austin, Austin, TX 78712

1. A. M. Dziewonski, D. L. Anderson, Preliminary reference Earth model. *Phys. Earth Planet. Inter.* **25**, 297–356 (1981).
2. J. Li, Y. Fei, “Experimental constraints on core composition” in *Treatise on Geochemistry*, K. K. Turekian, Ed. (Elsevier, Oxford, 2014), pp. 527–557.
3. Y. Zhang, J. F. Lin, Molten iron in Earth-like exoplanet cores. *Science* **375**, 146–147 (2022).
4. J. Aubert, C. C. Finlay, A. Fournier, Bottom-up control of geomagnetic secular variation by the Earth's inner core. *Nature* **502**, 219–223 (2013).
5. M. Landeau, J. Aubert, P. Olson, The signature of inner-core nucleation on the geodynamo. *Earth Planet. Sci. Lett.* **465**, 193–204 (2017).
6. H. Kraljić, T.-S. Pham, Shear properties of Earth's inner core constrained by a detection of *J* waves in global correlation wavefield. *Science* **362**, 329–332 (2018).
7. L. Vočadlo, Ab initio calculations of the elasticity of iron and iron alloys at inner core conditions: Evidence for a partially molten inner core? *Earth Planet. Sci. Lett.* **254**, 227–232 (2007).
8. Y. Li, L. Vočadlo, J. P. Brodholt, The elastic properties of hcp-Fe alloys under the conditions of the Earth's inner core. *Earth Planet. Sci. Lett.* **493**, 118–127 (2018).
9. G. N. Greaves, A. L. Greer, R. S. Lakes, T. Rouxel, Poisson's ratio and modern materials. *Nat. Mater.* **10**, 823–837 (2011).
10. H. K. Mao *et al.*, Phonon density of states of iron up to 153 gigapascals. *Science* **292**, 914–916 (2001).
11. C. A. Murphy, J. M. Jackson, W. Sturhahn, Experimental constraints on the thermodynamics and sound velocities of hcp-Fe to core pressures. *J. Geophys. Res.: Solid Earth* **118**, 1999–2016 (2013).
12. J. C. E. Irving, Earth's soft heart. *Science* **362**, 294–294 (2018).
13. F. Nimmo, “Energetics of the core” in *Treatise on Geophysics*, G. Schubert, Ed. (Elsevier, Oxford, 2015), vol. **8**, pp. 27–55.
14. A. Deuss, Heterogeneity and anisotropy of Earth's inner core. *Annu. Rev. Earth Planet. Sci.* **42**, 103–126 (2014).
15. T. Wang, X. Song, H. H. Xia, Equatorial anisotropy in the inner part of Earth's inner core from autocorrelation of earthquake coda. *Nat. Geosci.* **8**, 224–227 (2015).
16. S. Labrosse, J.-P. Poirier, J.-L. Le Mouél, On cooling of the Earth's core. *Phys. Earth Planet. Inter.* **99**, 1–17 (1997).
17. J. Li *et al.*, Shock melting curve of iron: A consensus on the temperature at the Earth's inner core boundary. *Geophys. Res. Lett.* **47**, e2020GL087758 (2020).
18. S. Anzellini, A. Dewaele, M. Mezouar, P. Loubeyre, G. Morard, Melting of iron at Earth's inner core boundary based on fast X-ray diffraction. *Science* **340**, 464–466 (2013).
19. S. J. Turneaure, S. M. Sharma, Y. M. Gupta, Crystal structure and melting of Fe shock compressed to 273 GPa: In situ x-ray diffraction. *Phys. Rev. Lett.* **125**, 215702 (2020).
20. R. G. Kraus *et al.*, Measuring the melting curve of iron at super-Earth core conditions. *Science* **375**, 202–205 (2022).
21. G. Morard *et al.*, Solving controversies on the iron phase diagram under high pressure. *Geophys. Res. Lett.* **45**, 11,074–11,082 (2018).
22. T. Sun, J. P. Brodholt, Y. Li, L. Vočadlo, Melting properties from ab initio free energy calculations: Iron at the Earth's inner-core boundary. *Phys. Rev. B* **98**, 224301 (2018).
23. D. Alfè, G. Price, M. Gillan, Iron under Earth's core conditions: Liquid-state thermodynamics and high-pressure melting curve from ab initio calculations. *Phys. Rev. B* **65**, 165118 (2002).
24. K. Hirose, B. Wood, L. Vočadlo, Light elements in the Earth's core. *Nat. Rev. Earth Environ.* **2**, 645–658 (2021).
25. J. G. Dash, A. W. Rempel, J. S. Wettlaufer, The physics of premelted ice and its geophysical consequences. *Rev. Mod. Phys.* **78**, 695–741 (2006).
26. A. Samanta, M. E. Tuckerman, T.-Q. Yu, W. E. Microscopic mechanisms of equilibrium melting of a solid. *Science* **346**, 729–732 (2014).
27. C. J. Wu, P. Söderlind, J. N. Glosli, J. E. Klepeis, Shear-induced anisotropic plastic flow from body-centred-cubic tantalum before melting. *Nat. Mater.* **8**, 223 (2009).
28. Y. Wang *et al.*, Electronically driven 1D cooperative diffusion in a simple cubic crystal. *Phys. Rev. X* **11**, 011006 (2021).
29. J.-F. Lin *et al.*, Sound velocities of hot dense iron: Birch's law revisited. *Science* **308**, 1892–1894 (2005).
30. B. Martorell, L. Vočadlo, J. Brodholt, I. G. Wood, Strong premelting effect in the elastic properties of hcp-Fe under inner-core conditions. *Science* **342**, 466–468 (2013).
31. C. Prescher *et al.*, High Poisson's ratio of Earth's inner core explained by carbon alloying. *Nat. Geosci.* **8**, 220–223 (2015).
32. Y. He *et al.*, Superionic iron alloys and their seismic velocities in Earth's inner core. *Nature* **602**, 258–262 (2022).
33. X. Sha, R. E. Cohen, First-principles thermal equation of state and thermoelasticity of hcp Fe at high pressures. *Phys. Rev. B* **81**, 094105 (2010).
34. X. Sha, R. E. Cohen, Elastic isotropy of e-Fe under Earth's core conditions. *Geophys. Res. Lett.* **37**, L10302 (2010).
35. S. Merkel, H. P. Liermann, L. Miyagi, H. R. Wenk, In situ radial X-ray diffraction study of texture and stress during phase transformations in bcc-, fcc- and hcp-iron up to 36 GPa and 1000 K. *Acta Mater.* **61**, 5144–5151 (2013).
36. A. E. Gleason, W. L. Mao, Strength of iron at core pressures and evidence for a weak Earth's inner core. *Nat. Geosci.* **6**, 571 (2013).
37. H.-R. Wenk, S. Matthies, R. Hemley, H.-K. Mao, J. Shu, The plastic deformation of iron at pressures of the Earth's inner core. *Nature* **405**, 1044 (2000).
38. S. Merkel, M. Gruson, Y. Wang, N. Nishiyama, C. N. Tomé, Texture and elastic strains in hcp-iron plastically deformed up to 17.5 GPa and 600 K: Experiment and model. *Model. Simul. Mater. Sci. Eng.* **20**, 024005 (2012).
39. M. C. Brennan *et al.*, High-pressure deformation of iron-nickel-silicon alloys and implications for Earth's inner core. *J. Geophys. Res.: Solid Earth* **126**, e2020JB021077 (2021).
40. W. Wang *et al.*, Strong shear softening induced by superionic hydrogen in Earth's inner core. *Earth Planet. Sci. Lett.* **568**, 117014 (2021).
41. A. B. Belonoshko *et al.*, Stabilization of body-centred cubic iron under inner-core conditions. *Nat. Geosci.* **10**, 312 (2017).
42. Z. Wu, W. Wang, Shear softening of earth's inner core as indicated by its high Poisson ratio and elastic anisotropy. *Fundam. Res.*, in press. 10.1016/j.fmre.2022.08.010.
43. M. Ghosh, S. Zhang, L. Hu, S. Hu, Cooperative diffusion in body-centered cubic iron in Earth and super-Earths' inner core conditions. *J. Phys. Condens. Matter* **35**, 154002 (2023).
44. S. Tateno, K. Hirose, Y. Ohishi, Y. Tatsumi, The structure of iron in Earth's inner core. *Science* **330**, 359–361 (2010).
45. S. Singh, M. Taylor, J. Montagner, On the presence of liquid in Earth's inner core. *Science* **287**, 2471–2474 (2000).
46. Y. Zhang, P. Nelson, N. Dygert, J.-F. Lin, Fe alloy slurry and a compacting cumulate pile across Earth's inner-core boundary. *J. Geophys. Res.: Solid Earth* **124**, 10954–10967 (2019).
47. J. M. Brown, R. G. McQueen, Phase transitions, Grüneisen parameter, and elasticity for shocked iron between 77 GPa and 400 GPa. *J. Geophys. Res.* **91**, 7485–7494 (1986).
48. J. H. Nguyen, N. C. Holmes, Melting of iron at the physical conditions of the Earth's core. *Nature* **427**, 339–342 (2004).
49. T. Sakamaki *et al.*, Constraints on Earth's inner core composition inferred from measurements of the sound velocity of hcp-iron in extreme conditions. *Sci. Adv.* **2**, e1500802 (2016).
50. D. Antonangeli *et al.*, Sound velocities and density measurements of solid hcp-Fe and hcp-Fe-Si (9 wt.%) alloy at high pressure: Constraints on the Si abundance in the Earth's inner core. *Earth Planet. Sci. Lett.* **482**, 446–453 (2018).
51. D. Ikuta *et al.*, Sound velocity of hexagonal close-packed iron to the Earth's inner core pressure. *Nat. Commun.* **13**, 7211 (2022).
52. C. S. Yoo, N. C. Holmes, M. Ross, D. J. Webb, C. Pike, Shock temperatures and melting of iron at Earth core conditions. *Phys. Rev. Lett.* **70**, 3931–3934 (1993).
53. H. Huang *et al.*, Inner core composition paradox revealed by sound velocities of Fe and Fe-Si alloy. *Nat. Commun.* **13**, 616 (2022).
54. Z. Mao *et al.*, Sound velocities of Fe and Fe-Si alloy in the Earth's core. *Proc. Natl. Acad. Sci. U.S.A.* **109**, 10239–10244 (2012).
55. X. Fan, D. Pan, M. Li, Melting of bcc crystal Ta without the Lindemann criterion. *J. Phys. Condens. Matter* **31**, 095402 (2019).
56. L. E. Dresselhaus-Marais *et al.*, In situ visualization of long-range defect interactions at the edge of melting. *Sci. Adv.* **7**, eabe8311 (2021).
57. L. Van Hove, Correlations in space and time and Born approximation scattering in systems of interacting particles. *Phys. Rev.* **95**, 249 (1954).
58. W. Sturhahn *et al.*, Phonon density of states measured by inelastic nuclear resonant scattering. *Phys. Rev. Lett.* **74**, 3832 (1995).
59. T. Komabayashi, Thermodynamics of the system Fe-Si-O under high pressure and temperature and its implications for Earth's core. *Phys. Chem. Miner.* **47**, 32 (2020).
60. T. Sakai *et al.*, Sound velocity measurements of hcp-Fe-Si alloy at high pressure and high temperature by inelastic X-ray scattering. *Am. Mineral.* **103**, 85–90 (2018).
61. S. Dominijanni *et al.*, Sound velocity measurements of B2-Fe-Ni-Si alloy under high pressure by inelastic X-ray scattering: Implications for the composition of Earth's core. *Geophys. Res. Lett.* **49**, e2021GL096405 (2022).
62. T. Sakai, E. Ohtani, N. Hirao, Y. Ohishi, Stability field of the hcp-structure for Fe, Fe-Ni, and Fe-Ni-Si alloys up to 3 Mbar. *Geophys. Res. Lett.* **38**, L09302 (2011).
63. T. Komabayashi *et al.*, Phase relations in the system Fe-Ni-Si to 200 GPa and 3900 K and implications for Earth's core. *Earth Planet. Sci. Lett.* **512**, 83–88 (2019).
64. J. K. Wicks *et al.*, Crystal structure and equation of state of Fe-Si alloys at super-Earth core conditions. *Sci. Adv.* **4**, eaao5864 (2018).
65. B. A. Buffett, Geodynamic estimates of the viscosity of the Earth's inner core. *Nature* **388**, 571–573 (1997).
66. Q. Liu, X. Zhou, X. Zeng, S. N. Luo, Sound velocity, equation of state, temperature and melting of LiF single crystals under shock compression. *J. Appl. Phys.* **117**, 045901 (2015).
67. X. Cao *et al.*, Refractive index and phase transformation of sapphire under shock pressures up to 210 GPa. *J. Appl. Phys.* **121**, 115903 (2017).
68. P. Renganathan, T. S. Duffy, Y. M. Gupta, Sound velocities in shock-compressed soda lime glass: Melting and liquid-state response. *Phys. Rev. B* **104**, 014113 (2021).
69. T. S. Duffy, T. J. Ahrens, Compressional sound velocity, equation of state, and constitutive response of shock-compressed magnesium oxide. *J. Geophys. Res.: Solid Earth* **100**, 529–542 (1995).
70. M. Beason, B. Jensen, S. Crockett, Shock melting and the hcp-bcc phase boundary of Mg under dynamic loading. *Phys. Rev. B* **104**, 144106 (2021).
71. H. Huang *et al.*, Evidence for an oxygen-depleted liquid outer core of the Earth. *Nature* **479**, 513–516 (2011).
72. H.-J. Huang, F.-Q. Jing, L.-C. Cai, Y. Bi, Grüneisen parameter along Hugoniot and melting temperature of e-iron: A result from thermodynamic calculations. *Chin. Phys. Lett.* **22**, 836–838 (2005).
73. J. M. Brown, J. N. Fritz, R. S. Hixson, Hugoniot data for iron. *J. Appl. Phys.* **88**, 5496–5498 (2000).
74. G. Kresse, J. Furthmüller, Efficient iterative schemes for ab initio total-energy calculations using a plane-wave basis set. *Phys. Rev. B* **54**, 11169–11186 (1996).
75. P. E. Blöchl, Projector augmented-wave method. *Phys. Rev. B* **50**, 17953 (1994).
76. J. P. Perdew, K. Burke, M. Ernzerhof, Generalized gradient approximation made simple. *Phys. Rev. Lett.* **77**, 3865–3868 (1996).
77. M. Parrinello, A. Rahman, Crystal structure and pair potentials: A molecular-dynamics study. *Phys. Rev. Lett.* **45**, 1196 (1980).
78. G. S. Grest, K. Kremer, Molecular dynamics simulation for polymers in the presence of a heat bath. *Phys. Rev. A* **33**, 3628 (1986).
79. L. Zhang, J. Han, H. Wang, R. Car, E. Weinan, Deep potential molecular dynamics: A scalable model with the accuracy of quantum mechanics. *Phys. Rev. Lett.* **120**, 143001 (2018).
80. H. Wang, L. Zhang, J. Han, E. Weinan, DeepPMD-kit: A deep learning package for many-body potential energy representation and molecular dynamics. *Comput. Phys. Commun.* **228**, 178–184 (2018).
81. L. Zhang, H. Wang, R. Car, E. Weinan, Phase diagram of a deep potential water model. *Phys. Rev. Lett.* **126**, 236001 (2021).
82. Y. Zhang *et al.*, DP-GEN: A concurrent learning platform for the generation of reliable deep learning based potential energy models. *Comput. Phys. Commun.* **253**, 107206 (2020).
83. S. Plimpton, Fast parallel algorithms for short-range molecular dynamics. *J. Comput. Phys.* **117**, 1–19 (1995).
84. A. B. Belonoshko, G. S. Smirnov, A comparison of experimental and ab initio structural data on Fe under extreme conditions. *Metals* **13**, 1096 (2023).
85. Y. Zhang *et al.*, Melting curve of vanadium up to 256 GPa: Consistency between experiments and theory. *Phys. Rev. B* **102**, 214104 (2020).
86. A. Togo, I. Tanaka, First principles phonon calculations in materials science. *Scr. Mater.* **108**, 1–5 (2015).
87. A. Carreras, A. Togo, I. Tanaka, DynaPhoPy: A code for extracting phonon quasiparticles from molecular dynamics simulations. *Comput. Phys. Commun.* **221**, 221–234 (2017).
88. W. Humphrey, A. Dalke, K. Schulten, VMD: Visual molecular dynamics. *J. Mol. Graph.* **14**, 33–38 (1996).
89. A. Stukowski, Visualization and analysis of atomistic simulation data with OVITO—the open visualization tool. *Model. Simul. Mater. Sci. Eng.* **18**, 015012 (2009).